

A Multi-Modal Fusion Platform for Joint Environment Sensing and Channel Sounding in Highly Dynamic Scenarios

Xuejian Zhang, *Graduate Student Member, IEEE*, Ruisi He, *Senior Member, IEEE*, Mi Yang, *Member, IEEE*, Zhengyu Zhang, *Graduate Student Member, IEEE*, Ziyi Qi

Abstract—6G system is evolving toward full-spectrum coverage, ultra-wide bandwidth, and high mobility, resulting in increasingly complex propagation environments. The deep integration of communication and sensing is widely recognized as a core 6G vision, underscoring the importance of comprehensive environment awareness. Accurate channel modeling forms the foundation of 6G system design and optimization, and channel sounders provide the essential empirical basis. However, existing channel sounders, although supporting wide bandwidth and large antenna arrays in selected bands, generally lack cross-band capability, struggle in dynamic scenarios, and provide limited environmental awareness. The absence of detailed environmental information restricts the development of environment-aware channel models. To address this gap, we propose a multi-modal sensing and channel sounding fusion platform that enables temporally and spatially synchronized acquisition of images, point clouds, geolocation information, and multi-band multi-antenna channel data. The modular architecture facilitates rapid deployment in diverse dynamic environments. The platform supports Sub-6 GHz and mmWave bands with up to 1 GHz bandwidth and 1 ns delay resolution, enabling multi-antenna measurements with a channel switching rate of 8 ms. Moreover, it achieves centimeter-level and 360° environmental sensing accuracy and meter-level positioning accuracy. Key performance metrics of the platform, including dynamic range, phase stability, delay resolution, and multi-modal data synchronization, are validated through vehicle-to-infrastructure measurement campaign. The established platform supports environment–channel joint modeling, enabling analysis and optimization of channel models in dynamic 6G scenarios.

Index Terms—6G, wireless propagation, channel sounder, multi-modal fusion sensing, highly dynamic scenarios.

I. INTRODUCTION

With growing interest from industry and academia, 6G is envisioned to deliver intelligent, ultra-reliable, low-latency services while enhancing spectrum efficiency and reducing costs [1]–[3]. Unlike previous generations that primarily emphasized communication performance, one of the core visions of 6G is the deep integration of communications, sensing, and artificial intelligence (AI), thereby enabling wireless systems with environment awareness and context-adaptive capabilities [4]–[6]. This paradigm shift raises a new research challenge: how to jointly exploit multi-modal sensing and channel information to build intelligent wireless systems that can deeply interact with the physical world [7].

Accurate channel modeling serves as a fundamental basis for 6G system design [8], [9]. In complex and highly dynamic

non-stationary scenarios, integrating multi-modal sensing with channel modeling enables more accurate characterization of spatiotemporal channel evolution and supports coordinated communication, sensing, and decision-making [10]. Multi-modal generally refers to the integration of heterogeneous data sources such as channel sounding signals, sensor-based environmental information, and geospatial data [11]. Cross-modal complementarity not only overcomes the limitations of single-modality approaches but also uncovers the intrinsic relationship between environment dynamics and channel evolution [12]. However, traditional channel modeling approaches, such as statistical methods, rely solely on communication signals, making it difficult to capture environmental variations and establish explicit environment–channel mappings [13], [14]. Therefore, how to effectively acquire and exploit multi-modal environmental sensing data to enhance channel modeling has emerged as a critical challenge in 6G research.

The rapid advancement of multi-modal sensing technologies provides a promising pathway [15], [16]. Devices such as LiDAR, RGB/depth cameras, inertial measurement units, and geographic information systems can deliver high-resolution and complementary descriptions of the surrounding environment [17], [18]. Since multi-modal sensing and communication data are collected from the same physical world, they exhibit strong spatio-temporal consistency and correlation [11]. By leveraging this consistency, a more comprehensive understanding of the environment can be achieved [19]. Nevertheless, there is still a lack of experimental platforms capable of systematically acquiring, aligning, and fusing such multi-modal data with precise spatio-temporal synchronization. Existing systems are typically designed only either for channel measurements or for sensing tasks, leading to fragmented interfaces, inconsistent timestamps, and incompatible data formats, which significantly hinder cross-domain research. Therefore, developing a multi-modal environmental sensing and channel sounding platform is of great scientific and engineering significance. Such a platform enables synchronized acquisition, unified calibration, and integrated fusion of multi-source sensing and communication data. It provides a solid foundation for studying the coupling mechanisms between environment and channel characteristics and facilitating intelligent channel modeling of integrated sensing and communication (ISAC) [20]–[22].

A. Related Work

Conventional channel sounders only transmit and receive signals, lacking the ability to capture environmental information simultaneously [38]. Recently, with the rise of sensing

X. Zhang, R. He, M. Yang, Z. Zhang, and Z. Qi are with the School of Electronics and Information Engineering and the Frontiers Science Center for Smart High-speed Railway System, Beijing Jiaotong University, Beijing 100044, China (email: 23115029@bjtu.edu.cn; ruisi.he@bjtu.edu.cn; myang@bjtu.edu.cn; 22115006@bjtu.edu.cn; 21111040@bjtu.edu.cn).

TABLE I
COMPARISON OF RELATED WORKS ON ENVIRONMENT SENSING AND CHANNEL SOUNDING PLATFORM.

Ref.	Scenarios	Environment Sensing data			Channel Sounding data				Mobility	Sounder Type
		Image	Point Cloud	Geolocation	Freq.	Bandwidth	Antenna Setup	Waveform		
[23]	Indoor ISAC	×	×	×	5-6 GHz	400 MHz	128×16 MIMO	ZC	Low Speed	USRP
[24]	UMi/O2I	×	×	×	4-6 GHz	180 MHz	SISO	PN	Low Speed	USRP
[25]	Indoor	×	×	×	3-18 GHz	1 GHz	SISO	Multi-Tone	5 km/h	NI PXIe
[26]	Indoor	×	×	×	28 GHz	2 GHz	128×256 MIMO	ZC	0.36 km/h	NI PXIe
[27]	UMi	×	×	×	28 GHz	400 MHz	16×16 MIMO	Multi-Tone	×	NI PXIe
[28]	Indoor	×	×	×	28-30 GHz	200 MHz	1×360 SIMO	CW	×	VNA
[29]	Indoor ISAC	×	×	×	28 GHz	2 GHz	Rotating-Mirror	ZC	×	FPGA Board
[30]	V2V	×	×	✓	26.5-40 GHz	320 MHz	4×4 MIMO	PN	60 km/h	Keysight
[31]	A2G	×	×	✓	2.4/3.5 GHz	100 MHz	1×8 SIMO	ZC	7.2 km/h	NI PXIe
[32]	V2I	×	×	✓	3.5 GHz	100 MHz	SISO	5G	40 km/h	USRP
[33]	UMi	×	×	✓	3.5-3.6 GHz	122.88 MHz	1×16 SIMO	5G	Low Speed	USRP
[34]	UMi/O2I	×	×	✓	3-40 GHz	200/1000 MHz	SISO	PN	Low Speed	R & S
[35]	UMa/UMi	✓	×	×	24/60 GHz	200/400 MHz	4×4 SIMO	Multi-Tone	×	FPGA Board
[36]	Indoor ISAC	✓	✓	✓	28/60 GHz	2 GHz	8×16 MIMO	PN	Low Speed	FPGA Board
[37]	V2I/V2V	✓	✓	✓	60 GHz	N/A	1×64 SIMO	N/A	10-50 km/h	FPGA Board

Notes: PN: Pseudo-Noise sequence, ZC: Zadoff-Chu sequence, CW: Continuous Wave. VNA: Vector Network Analyzer, UMi: Urban Microcell, UMa: Urban Macrocell, O2I: Outdoor-to-Indoor, V2I: Vehicle-to-Infrastructure.

devices, integrated platforms combining channel sounding and multi-modal sensing have emerged, enabling more intelligent and efficient environment-aware channel modeling [15]. A summary of related work is provided in Table I.

A variety of channel sounders have emerged based on different hardware architectures, sounding waveforms, antenna configurations, and operating frequency bands. For example, [23] and [24] propose multiple-input multiple-output (MIMO) and single-input single-output (SISO) channel sounders based on universal software radio peripherals (USRPs), covering 5–6 GHz and 4–6 GHz with bandwidths of 400 MHz and 180 MHz, respectively. A 3–18 GHz sounder with 1 GHz bandwidth supporting low-mobility measurements is presented in [25]. Building upon wideband sounder designs, [26] implements a 128×256 massive MIMO channel sounder at 28 GHz on the National Instruments PCI eXtensions for Instrumentation Express (NI PXIe) architecture, achieving up to 2 GHz bandwidth and 0.5 ns delay resolution. Sounders in [27], [28] also operate at 28 GHz for MIMO and SIMO configurations, but provide only 400 MHz and 200 MHz bandwidth and lack mobility support. An alternative mmWave sounder in [29] replaces electronic switches and antenna arrays with a field-programmable gate array (FPGA)-controlled rotating mirror to enable 2 GHz bandwidth, but is still mobility-limited. Despite their merits in wideband and MIMO sounding, existing platforms generally operate over a single band and offer limited mobility support, restricting their applicability to indoor or low-mobility scenarios. Crucially, they do not capture environmental information, falling short of the integrated sensing-communication requirements envisioned for 6G.

To enable outdoor dynamic measurements, geolocation information has recently been incorporated. For instance, A Keysight-based 4×4 MIMO sounder for vehicle-to-vehicle (V2V) scenarios covering 26.5–40 GHz is reported in [30], while a 2.4/3.5 GHz single-input multiple-output (SIMO)

sounder for air-to-ground (A2G) scenarios is introduced in [31]. Passive channel sounders capable of receiving commercial 5G downlink signals are introduced in [32] and [33] using USRPs. Although these sounders support higher mobility and can exploit geolocation information, their usable frequency bands remain limited. The 3–40 GHz sounder in [34] extends frequency coverage, yet lacks multi-antenna support and still omits environmental information. The sounder in [34] extends frequency coverage, covering 3–40 GHz with up to 1 GHz bandwidth, yet lacks multi-antenna support and still omits environmental information.

Recent studies attempt to integrate environmental sensing into sounding platforms. In [35], a panoramic camera is incorporated into a 24/60 GHz double-directional channel sounder to capture environmental imagery, yet without mobility support. The platforms proposed in [36] and [37] integrate multi-modal environmental information (e.g., images, point clouds, and geolocation data) with channel sounding in the mmWave band, supporting wide bandwidth and multi-antenna measurements. However, both remain limited to a single operating frequency (e.g., 28/60 GHz). Moreover, [36] does not support highly dynamic channel measurements, while [37] only acquires beamforming power measurements rather than full channel impulse responses.

In summary, although existing channel sounders based on diverse hardware architectures have achieved notable wideband measurement capability and large-scale array support in certain key frequency bands, several limitations remain. First, most platforms operate on a single band and lack flexibility for multi-band or cross-band measurements, which restricts their applicability in the heterogeneous spectrum environment anticipated for 6G. Second, mobility support is still insufficient, particularly in highly dynamic outdoor scenarios, resulting in limited ability to capture realistic non-stationary channel characteristics. Third, environmental awareness is

largely absent or underutilized, since current platforms either rely on basic geographic information or have not yet achieved effective fusion of multi-modal sensing with high-resolution channel measurements. These limitations substantially impede the advancement of channel sounding technologies towards 6G ISAC, as they fail to yield channel characteristics that are simultaneously wideband, mobility-robust, and environment-aware. Therefore, the development of a new channel sounding platform that supports synchronized environmental sensing and channel measurement in real mobile scenarios, while maintaining low cost, real-time capability, strong adaptability, and high system integration, remains a pressing research need.

B. Contributions

To bridge this gap, this paper proposes a multi-modal integrated platform that enables synchronized environmental sensing and channel sounding, and further supports physical environment reconstruction and channel modeling in dynamic scenarios. The main contributions of this paper are summarized as follows.

- We develop an environment sensing and channel sounding platform that integrates multi-modal sensing data, enabling time- and space-synchronized acquisition of real-world images, point clouds, geolocation data, and channel sounding signals.
- The platform covers both Sub-6 GHz and mmWave frequency bands, supporting up to 1 GHz bandwidth, 1 ns delay resolution, and SIMO measurements. Point cloud and image data are jointly processed to enable environmental sensing with centimeter-level accuracy and full 360° coverage.
- The platform adopts a modular and extensible design, allowing flexible selection of sensing modalities according to different application needs. This design enables rapid adaptation to diverse dynamic environments and facilitates the construction of high-quality joint environment–channel databases.

The remainder of this paper is organized as follows. Section II describes the architecture of multi-modal fusion Sensing system. Sections III and IV introduce the design and implementation of channel sounding subsystem and visual sensing subsystem, respectively. Then in Section V, the performance indicators of proposed platform are verified and a sample measurement campaign is presented in Section VI. Finally, Section VII draws the conclusions.

II. ARCHITECTURE OF MULTI-MODAL ENVIRONMENT SENSING AND CHANNEL SOUNDING PLATFORM

A. Architecture of Platform

Fig. 1 illustrates the overall architecture of the proposed environment sensing and channel sounding platform, which consists of two subsystems: channel sounding subsystem and visual sensing subsystem. Channel sounding subsystem captures channel data after electromagnetic waves propagate wirelessly, while visual sensing subsystem collects intuitive representations of physical environment. Both subsystems also record geospatial data to specify the measurement locations.

Integrated hardware of the platform is shown in Fig. 2. To support multi-band measurements without increasing hardware complexity, channel sounding subsystem is implemented on NI hardware with two distinct architectures. Sub-6 GHz sounder employs a vector signal generator/analyizer (VSG/VSA), while the mmWave sounder is based on intermediate-frequency direct sampling using FlexRIO. Several antenna arrays operating at representative frequencies enable multi-antenna measurements to obtain spatio-temporal-frequency domain channel data. Geolocation information is provided by Global Navigation Satellite System (GNSS) antennas synchronized with rubidium clocks. More details of this subsystem are presented in Section III. Visual sensing subsystem integrates panoramic camera and LiDAR to acquire image and point cloud data of the same environment, which are spatially registered via a real-time fusion algorithm. LiDAR connects to the receiver host computer via Ethernet for synchronized triggering, while the camera links to a smartphone via Bluetooth to obtain time, velocity, and location data. The detailed design of this subsystem is described in Section IV.

Given the use of heterogeneous devices, strict synchronization across modalities is essential. To ensure both spatial and temporal alignment, four synchronization schemes are implemented: portable integrated hardware design, geospatial location matching, millisecond-level timestamp synchronization, and multi-frame image registration, as detailed in Section II-C. After synchronization, the collected multi-modal data, comprising channel data, geolocation data, image data, and point cloud data, form a unified dataset that jointly characterizes the electromagnetic and physical environments. This dataset is then processed to extract multipath parameters, reconstruct the 3D environment, and perform environment-aware channel modeling. This completes an end-to-end workflow from data acquisition and synchronization to fusion and modeling, enabling comprehensive characterization of wireless channels in dynamic scenarios.

B. Synchronization of Multi-Modal Data

Ensuring the usability of multi-modal data requires temporal synchronization for proper alignment across devices and spatial synchronization for mapping into a unified 3D coordinate system [39]. Temporal synchronization is achieved by estimating offsets and drift rates relative to a rubidium clock, chosen as the global reference, because different devices operate with independent clocks [36]. LiDAR operates at 10 Hz, while camera supports up to 100 Hz image acquisition. Rx captures channel data at up to 50 snapshots/s when actively triggered by PXIe-6674T in SIMO mode. Geolocation data are sampled at up to 120 Hz, with timestamps synchronized by rubidium clock. LiDAR connects via Ethernet for direct timestamp alignment with Rx, while the camera is synchronized through a Bluetooth-linked smartphone with Internet-synced time. This multi-frame registration mechanism temporally aligns consecutive LiDAR and image frames and spatially registers them into a unified coordinate system. Due to differing sampling rates, data volumes vary, interpolation or extrapolation is necessary in specific applications.

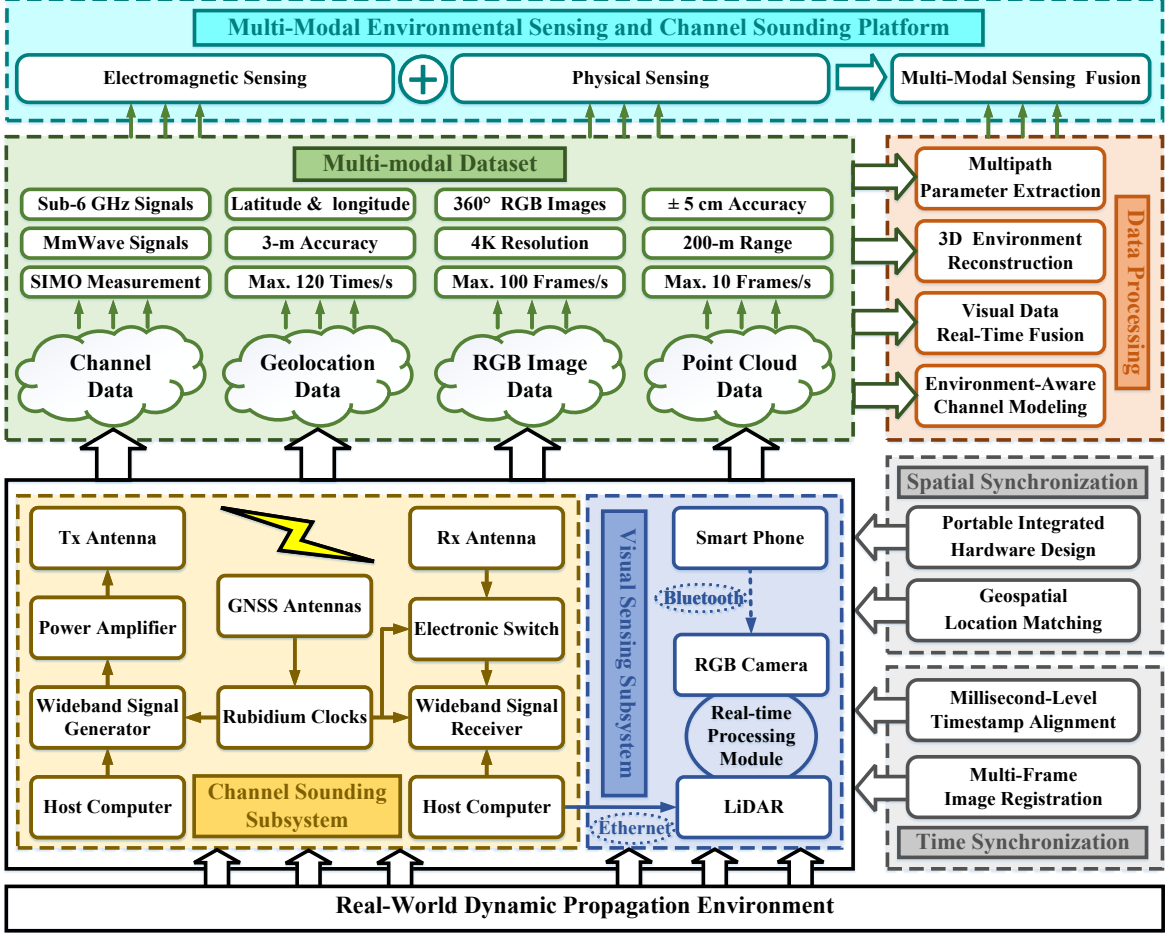


Fig. 1. Architecture of multi-modal environment sensing and channel sounding platform.

For spatial synchronization, we design a circular magnetic mount with a unified interface and dedicated extension brackets to rigidly integrate heterogeneous devices. Generally, to avoid occlusion, LiDAR and camera are elevated on a bracket, with camera mounted directly above LiDAR, ensuring unobstructed LiDAR scanning and full 360° image capture. Antennas are installed in front of LiDAR on a separate bracket attached to the mount; its lower height prevents interference with either line-of-sight (LoS) propagation or environmental sensing. GNSS antenna is positioned directly behind the LiDAR and aligned with Rx antennas in the same horizontal plane. In fact, without the need for spatial synchronization of multimodal data, each device could be freely mounted anywhere on the disk. The design also allows for other sensing devices to be installed using customized brackets with the same mechanical interface.

C. Platform Specifications

The proposed multi-modal environment sensing and channel sounding platform integrates wideband sounders, a LiDAR, and panoramic cameras to enable high-precision, spatiotemporally synchronized data acquisition. The channel sounding subsystem covers 10 MHz–6.6 GHz and 27–29 GHz bands, with maximum transmit powers of 47 dBm and 65 dBm,

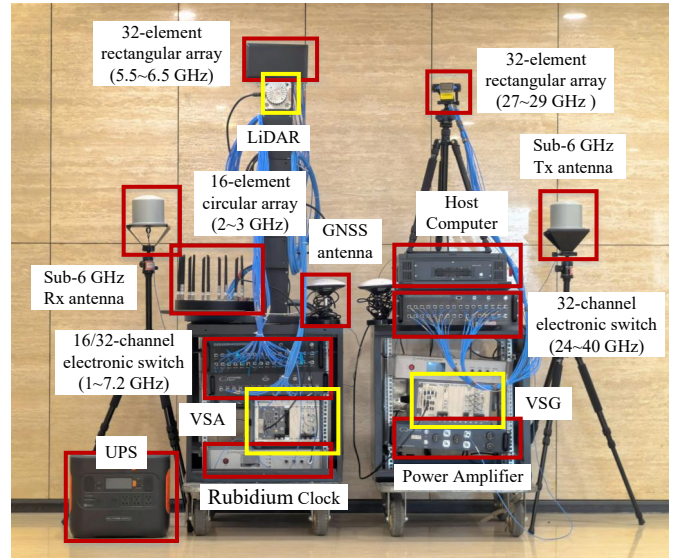


Fig. 2. Integrated hardware of established platform.

and bandwidths up to 1 GHz. It supports up to 100 channel snapshots/s with a minimum electronic switching interval of 8 microseconds for SIMO measurements, ensuring fine temporal resolution. The visual sensing subsystem employs a LiDAR

TABLE II
KEY SPECIFICATIONS OF THE PROPOSED PLATFORM.

Radio Frequency Performance Metrics		
Frequency Bands	10 MHz-6.6 GHz	27 GHz-29 GHz
Bandwidth	50 MHz	1 GHz
Delay Resolution	20 ns	1 ns
Dynamic Range	123.6 dB	128.2 dB
Antenna Array	16/32-element	
Transmit Power	Max. 47 dBm	Max. 65 dBm
Switching Interval	8 microseconds	
Acquisition Rate	100 snapshots/s	50 snapshots/s
Environment-Aware Sensing Metrics		
Number of Beams	128	
Scanning Accuracy	± 5 cm	
Scanning Range	200 m	
Field of View	360° (H) \times 45° (V)	
Image Resolution	Max. 4K	
Point Cloud Frame Rate	10 Hz	
Image Frame Rate	100 Hz	
Additional Parameters	velocity, altitude, acceleration	
Geolocation and Synchronization Metrics		
Positioning bands	L1 (1575.42 MHz), B1 (1561.098 MHz)	
Positioning Accuracy	± 3 m	
Position Update Rate	Max. 120 Hz	
Timing Stability	$\leq 1E-12$	
Supported Mobility	≥ 100 km/h	

and a camera. The LiDAR achieves a 200 m range with ± 5 cm accuracy at 10 frames/s, while the camera captures 4K photos at up to 100 frames/s. The platform achieves centimeter-level positioning accuracy and a 120 Hz update rate, providing a robust hardware foundation for multi-modal synchronization and environment-aware channel modeling. The detailed parameter specifications are listed in Table II, while the descriptions and validations of each subsystem are presented in detail in Sections III, IV, and V, respectively.

III. CHANNEL SOUNDING SUBSYSTEM DESIGN AND IMPLEMENTATION

A. Overall Architecture

The channel sounding subsystem is primarily designed to generate, transmit, and receive vector sounding signals across multiple frequency bands for electromagnetic environment sensing. The overall architecture of the subsystem is illustrated in Fig. 1. Its core components include a wideband signal generator and receiver. At the transmitter (Tx) side, the generated wideband signal is amplified by a power amplifier (PA) and radiated into wireless channel through Tx antenna. At the receiver (Rx) side, the signal is captured and amplified by a low-noise amplifier (LNA), and optionally switched across multiple channels via high-speed electronic switches to enable time-division multiplexed SIMO measurements. The received signal is then recorded as IQ data for offline processing. Time synchronization and positioning are ensured by rubidium clocks disciplined by GNSS reference.

To achieve cross-band and large-bandwidth channel sounding capability, two types of architectures are implemented.

The first is a Sub-6 GHz sounder based on VSG and VSA, while the second adopts an intermediate frequency (IF) direct-sampling structure with a FlexRIO framework, combined with up/down converters, to enable measurements in the mmWave band with up to 1 GHz bandwidth. By integrating these two architectures, the subsystem supports channel measurements from 10 MHz to 6.6 GHz and from 27 GHz to 28 GHz, achieving a maximum bandwidth of 1 GHz and a delay resolution of 1 ns. These capabilities provide a solid foundation for multi-band electromagnetic environment sensing and non-stationary channel modeling.

B. Sounding Waveform

Channel sounding transmits a known waveform and processes the received signal to extract the channel transfer function and impulse response [23]. Extending this to multiple antenna pairs enables spatial and directional characterization [40]. In this work, a multi-tone signal is adopted as baseband waveform, expressed as [27]:

$$m(t) = \sum_{n=-N}^N e^{j(2\pi n \Delta f t + \theta_n)}, \quad (1)$$

where Δf is the tone spacing, $2N+1$ is the number of tones, and θ_n is the phase of the n -th tone. Out-of-band subcarriers are zeroed to confine power within the effective bandwidth, and the frequency-domain signal is converted to the time domain via inverse fast fourier transform (IFFT). The resulting waveform exhibits a flat spectral profile, ensuring equal signal-to-noise Ratio (SNR) across all tones and enabling accurate, unbiased channel estimation.

C. Sounder Implementation

The core modules of both Sub-6 GHz and mmWave channel sounders are NI PXIE-based and programmed in LabVIEW. Key auxiliary components, such as electronic switches, power amplifiers, and rubidium clocks, are custom-designed to meet performance requirements and ensure flexibility.

Taking the 28 GHz mmWave sounder as an example, Fig. 3 shows the system architecture. At Tx, a PXIE-5745 wideband signal generator produces the baseband probing waveform, which is then upconverted by a customized module. This module performs two-stage frequency conversion (1.3–2.3 GHz \rightarrow 4.5–5.5 GHz \rightarrow 27.5–28.5 GHz), followed by power amplification and radiation via a horn antenna. On the receiver side, signals are collected by a 32-element antenna array through a high-speed 32-channel electronic switch and processed by a custom downconverter integrated with the switch in a 2U chassis. After filtering and low-noise amplification, the signal is downconverted back to 1.3–2.3 GHz and digitized by a PXIE-5775 wideband digitizer for storage and post-processing. Both upconversion and downconversion modules adopt a modular design, allowing reconfiguration by replacing mixers or power amplifiers to adjust frequency, bandwidth, or output power, thereby improving adaptability and reducing maintenance complexity. System synchronization is achieved using a GNSS-disciplined rubidium clock and a PXIE-6674T

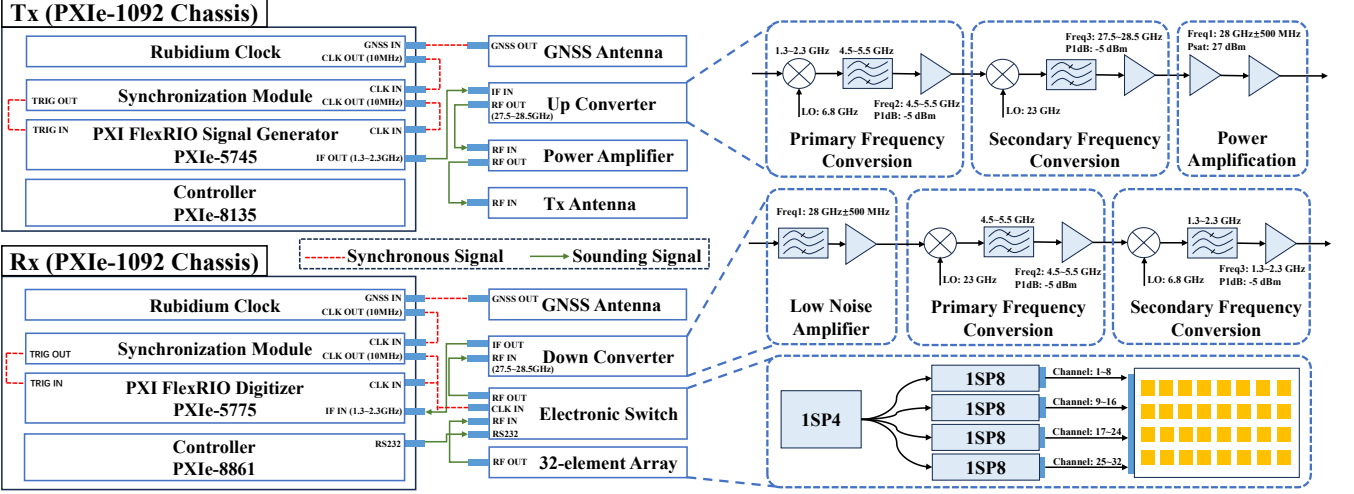


Fig. 3. Design and implementation of mmWave channel sounder.

timing module, which provide stable 10 MHz reference clocks and 1 pulse per second (PPS) trigger signals. The 10 MHz clock maintains phase coherence across all modules, while the UTC-aligned 1 PPS ensures simultaneous triggering at Tx and Rx, even when geographically separated.

D. Sounder Hardware

The integrated channel sounding system supports both Sub-6 GHz and mmWave bands, enabling flexible and high-fidelity measurements in dynamic scenarios. A photo of the hardware setup is shown in Fig. 2, and the key specifications are summarized in Table III. The major hardware modules are outlined as follows.

1) *VSA and VSG*. The VSG and VSA are implemented using PXIe-5673 and PXIe-5663 modules, supporting the Sub-6 GHz band. Two rubidium clocks provide high-stability timing and synchronization across all modules, which are housed within a PXIe-1092 chassis. The Sub-6 GHz system supports operation up to 6.6 GHz with a maximum bandwidth of 50 MHz. In SISO mode, the platform achieves a maximum snapshot acquisition rate of 240 snapshots/s, while in SIMO mode, the maximum snapshot rate reaches 100 snapshots/s.

2) *FlexRIO Signal Generator and Digitizer*. PXIe-5745/5775 modules are utilized, featuring a wideband IF direct-acquisition and high-speed digital-to-analog conversion architecture for wideband signal generation and capture with up to 1 GHz bandwidth. Combined with external up/down converters, they can support mmWave channel measurements. During SIMO measurements, a maximum snapshot acquisition rate of 50 snapshots/s is achieved. Moreover, PXIe-5745/5775/6674T can also be integrated into PXIe 1092 chassis, significantly saving hardware space.

3) *Power Amplifier*. To ensure a higher SNR in both Sub-6 GHz and mmWave bands, two high-power amplifiers are employed. The Sub-6 GHz amplifier offers a gain of 47.5 ± 5 dB, with a saturated output power (P_{sat}) of at least 47.5 dBm and a 1 dB compression point (P1dB) of 45 dBm. The mmWave amplifier provides a gain of 47 ± 5 dB, with a P_{sat} of

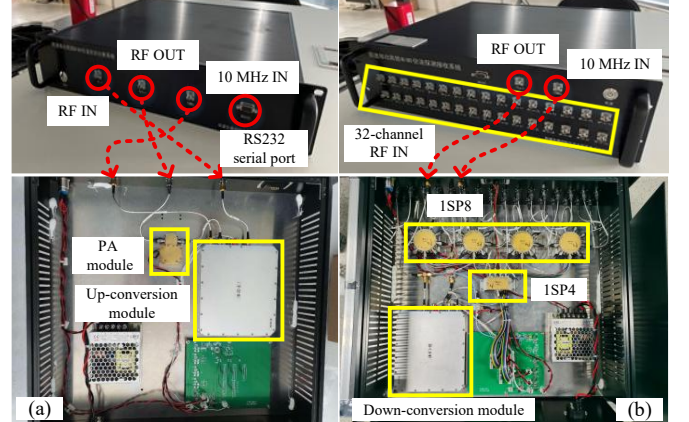


Fig. 4. (a) Up converter; (b) Down converter and electronic switch.

no less than 45 dBm and a P1dB of 43 dBm. Key performance specifications are summarized in Table III.

4) *Electronic Switch*. The system adopts a SIMO architecture, where a high-speed switch time-division multiplexes array elements. The custom-designed electronic switch, illustrated in Figs. 2 and 3. Taking the 32-channel mmWave electronic switch as an example, the minimum switching interval between adjacent channels is 8 microseconds and the switching interval can also be flexibly configured via the host computer. The insertion loss is around 12 dB. In addition, a two-stage cascaded control structure is adopted, where a single-pole four-throw (1SP4) module governs four single-pole eight-throw (1SP8) submodules, collectively enabling 32 independent RF channels. It reduces hardware complexity and cost, and enables compact, scalable integration.

5) *Rubidium Clock*. Accurate synchronization is achieved with GNSS-disciplined rubidium clocks, which provide 10 MHz reference and 1 PPS signals to Tx/Rx timing modules, ensuring frequency and phase coherence without cabled connections during measurements. The GNSS discipline also supplies real-time positioning (≤ 3 m accuracy), enabling site-

TABLE III
KEY HARDWARE COMPONENTS OF CHANNEL SOUNDING SYSTEM

Type	Model	Description
VSG	NI PXIe-5673	Freq: 50 MHz–6.6 GHz, Modulation bandwidth >100 MHz
VSA	NI PXIe-5663	Freq: 10 MHz–6.6 GHz, Max. BW: 50 MHz, IQ sampling rate: 150 MS/s
FlexRIO Signal Generator	NI PXIe-5745	Freq: 1 MHz–3.2 GHz, BW: 60 MHz–2.85 GHz, IQ sampling rate: 12-bit, 6.4 GS/s
FlexRIO Digitizer	NI PXIe-5775	Freq: 1 MHz–6 GHz, BW: 500 KHz–6 GHz, IQ sampling rate: 12-bit, 6.4 GS/s
Synchronization Module	NI PXIe-6674T	Distributes a shared 10 MHz reference and trigger signals for precise Tx/Rx synchronization
Controller	NI PXIe-8135	2.3 GHz dual-core CPU, Intel Core i7, 16 GB RAM, 512 GB HDD
	NI PXIe-8861	2.8 GHz quad-core CPU, Intel Xeon Processor E3-1515M v5, 32GB RAM, 1 TB HDD
Power Amplifier	HRTY-010060G-60W	Freq: 1 GHz–6 GHz, $P_{sat}=47.5$ dBm, P1dB=45 dBm, 47.5 dB ± 5 dB gain
	LDPA27G36G30	Freq: 27–36 GHz, $P_{sat}=45$ dBm, P1dB=43 dBm, 45 dB ± 2 dB gain
Electronic Switch	Custom-designed	Freq: 2–3 GHz, 16 channels, Min switching cycle 8 ns, Insertion loss 4.5 dB
	Custom-designed	Freq: 5.4–6.4 GHz, 32 channels, Min switching cycle 8 ns, LNA: 30 dB gain, Insertion loss 8 dB
	Custom-designed	Freq: 24 GHz–40 GHz, 32 channels, Min switching cycle 8 ns, Insertion loss 10 dB
Up-Converter	Custom-designed	Two conversions: 1.3–2.3 GHz → 4.5–5.5 GHz → 27.5–28.5 GHz
Down-Converter	Custom-designed	Two conversions: 27.5–28.5 GHz → 4.5–5.5 GHz → 1.3–2.3 GHz
Rubidium Clock	SYN3204	10MHz and 1 PPS output, amplitude $\geq 0.5V$, stability after taming: $\leq 1E-12$

specific channel modeling.

6) *Synchronization Module.* The PXIe-6674T serves as the central timing and synchronization controller for the platform. It provides a high-stability 10 MHz reference clock, which can be phase-aligned to external GNSS-disciplined sources or an internal oven-controlled crystal oscillator (OCXO), ensuring accurate time base across all NI PXIe modules. By distributing a coherent clock and synchronized triggers, the PXIe-6674T ensures that multi-band channel sounding signals are captured coherently, supports accurate timestamping of IQ samples, and facilitates reliable integration of geolocation data. This capability is essential for maintaining measurement consistency across different frequency bands and multi-modal data sources.

7) *Up/down converter.* Since the PXIe-5745/5775 modules operate only at baseband or IF, external up- and down-converters are required to translate signals between the IF domain and the mmWave band. Custom dual-conversion modules are employed for this purpose, as summarized in Table III. For improved system integration, the up- and down-converters are embedded within mmWave power amplifier and electronic switch modules, respectively, as illustrated in Fig. 4.

8) *Antennas.* Tx employs omnidirectional antennas in Sub-6 GHz and horn antennas in mmWave to compensate for high-frequency loss. To meet diverse requirements, we have developed multiple array configurations, as shown in Fig. 2. Specifically, we design a 16-element circular array operating in the 2–3 GHz band to support standardized 5G-for-railway (5G-R) channel measurements. For V2V scenarios centered at 5.9 GHz and for mmWave communications, we employ two 32-element rectangular arrays covering 5.5–6.5 GHz and 27–29 GHz, respectively. These arrays achieve fast channel switching through customized electronic switches, thereby realizing SIMO channel measurements.

IV. VISUAL SENSING SUBSYSTEM DESIGN AND IMPLEMENTATION

The visual sensing subsystem is a crucial component of the multi-modal platform, designed to capture the geometric structure and semantic information of physical propagation environment. This subsystem works in concert with the channel sounder to provide rich contextual data, allowing a deeper understanding of the intricate relationships between the environment and characteristics of wireless channel. This section details the architecture, hardware implementation, and data processing methodologies of the visual sensing subsystem.

A. Overall Architecture

The primary function of the visual sensing subsystem is to provide a high-fidelity, spatio-temporally aligned digital representation of the measurement environment. This serves as the physical ground truth for analyzing radio propagation phenomena, such as identifying key scatterers, classifying LoS and non-line-of-sight (NLoS) conditions, and extracting environment-specific features for channel modeling.

The general architecture of the visual sensing subsystem is depicted in Fig. 5. It is composed of hardware and software layers. The hardware layer comprises two main modules: a LiDAR scanning module for 3D geometric reconstruction and an image acquisition module for capturing visual and semantic information. The LiDAR is connected to and controlled by the computer via an Ethernet cable, while the camera, although unable to establish a direct connection with the computer, is linked and controlled through a Bluetooth connection with a smartphone. The radar and camera obtain timing and positioning information from computer and smartphone, respectively. Therefore, as long as smartphone and computer remain Internet-synchronized, the point cloud data and image data can be consistently acquired with both temporal and

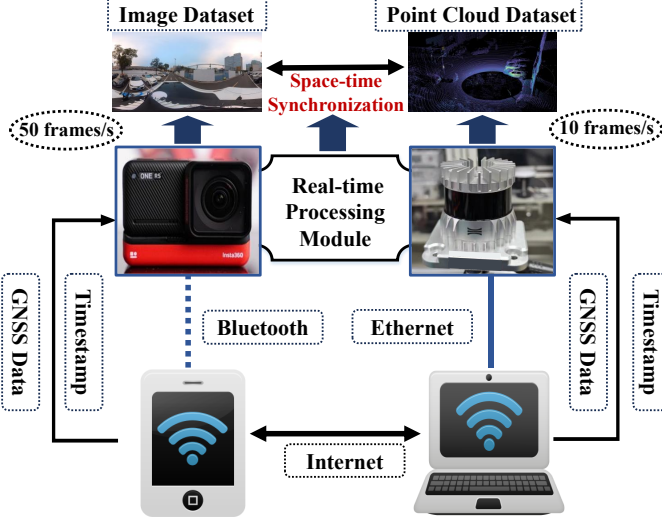


Fig. 5. System architecture of the environmental perception and reconstruction subsystem.

spatial alignment. The entire hardware setup is powered by a centralized supply unit.

The software layer, primarily built upon the Robot Operating System (ROS), manages hardware drivers, data acquisition, and real-time processing. Raw data streams, including point clouds from LiDAR, panoramic images from the camera, and pose information (position and orientation), are collected and pre-processed. These processed data form a digital representation of the environment. This dataset is then used for tasks such as instance segmentation, scatterer identification, and estimation of physical and electromagnetic parameters of environmental objects.

B. Hardware Configuration

To achieve high-precision and robust environment reconstruction, we have selected state-of-the-art sensing hardware and implemented a tightly-coupled LiDAR-inertial odometry framework for simultaneous localization and mapping (SLAM). The core components of the visual sensing subsystem are a high-resolution LiDAR and a versatile panoramic camera. Their key specifications are summarized in Table II.

The LiDAR scanning module is built around the OUSTER OS1-128-REV7, a 128-beam LiDAR sensor. It offers a 360° horizontal and 45° vertical field of view, enabling comprehensive environmental coverage. With a measurement accuracy of ± 5 cm and a range of up to 200 meters, it can rapidly and precisely capture the geometry of the surrounding environment. The module is integrated with a high-performance processing unit and a portable display, allowing for real-time visualization, multi-frame registration, and loop closure detection of the point cloud data [41]. This immediate feedback ensures the validity and utility of the collected data during measurement campaigns. The video and image acquisition module utilizes the Insta360 ONE RS, a modular camera system. Its 4K Wide Angle Lens, featuring a 1/2-inch 48MP CMOS sensor, supports up to 4K photos. For dynamic measurement scenarios,

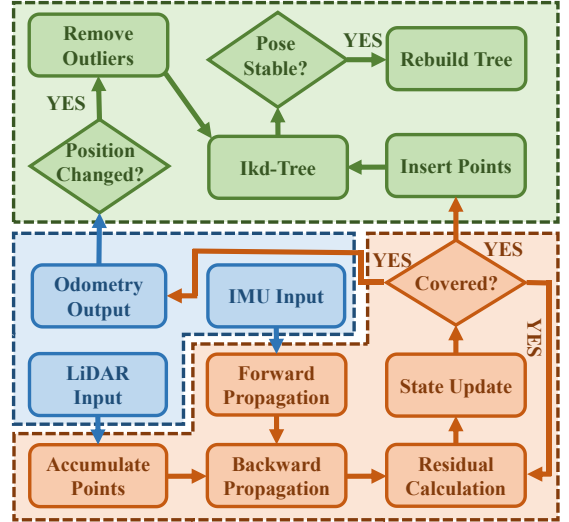


Fig. 6. System architecture of the LiDAR-inertial odometry framework. In the selection structure, if the input result is "NO," the state remains unchanged. For simplicity, this case is omitted in the figure.

an active high dynamic range (HDR) mode combined with FlowState stabilization ensures high-quality, stable footage.

C. Environment Reconstruction Implementation

To construct a globally consistent map of the environment, we employ a tightly-coupled LiDAR-inertial SLAM algorithm, the architecture of which is shown in Fig. 6. This approach fuses high-frequency inertial measurements from an inertial measurement unit (IMU) with lower-frequency, feature-rich LiDAR scans to achieve robust and accurate state estimation.

The state vector \mathbf{x} to be estimated includes the system's rotation \mathbf{R} , position \mathbf{p} , velocity \mathbf{v} , and the IMU biases for the gyroscope \mathbf{b}_g and accelerometer \mathbf{b}_a . The state propagation is driven by the IMU measurements. Between two consecutive LiDAR scans, the system state is predicted forward in time using the IMU kinematic model:

$$\dot{\mathbf{R}}(t) = \mathbf{R}(t)[\boldsymbol{\omega}_m(t) - \mathbf{b}_g(t)] \times \quad (2)$$

$$\dot{\mathbf{p}}(t) = \mathbf{v}(t) \quad (3)$$

$$\dot{\mathbf{v}}(t) = \mathbf{R}(t)(\mathbf{a}_m(t) - \mathbf{b}_a(t)) + \mathbf{g}, \quad (4)$$

where $[\cdot] \times$ is the skew-symmetric matrix operator, $\boldsymbol{\omega}_m(t)$ and $\mathbf{a}_m(t)$ are the raw gyroscope and accelerometer measurements, and \mathbf{g} is the gravity vector.

Upon the arrival of a new LiDAR scan, the points in the scan are used to form measurement residuals. These residuals quantify the discrepancy between measured points and existing map, which is built from previous scans. The core of the algorithm is to minimize a cost function that incorporates both IMU propagation errors and LiDAR measurement residuals:

$$\min_{\mathbf{x}} \left\{ \sum_{i \in \mathcal{I}} \|\mathbf{r}_{\mathcal{I}}(\hat{\mathbf{z}}_i, \mathbf{x})\|_{\mathbf{P}_i^{-1}}^2 + \sum_{j \in \mathcal{L}} \|\mathbf{r}_{\mathcal{L}}(\hat{\mathbf{z}}_j, \mathbf{x})\|_{\mathbf{Q}_j^{-1}}^2 \right\}, \quad (5)$$

where $\mathbf{r}_{\mathcal{I}}$ and $\mathbf{r}_{\mathcal{L}}$ represent the residual functions for the IMU and LiDAR measurements, respectively, with \mathbf{P} and \mathbf{Q} being

their corresponding covariance matrices. This non-linear least-squares problem is solved iteratively. The algorithm back-propagates the LiDAR-derived corrections to refine the state trajectory and update the IMU biases.

For efficient map management and real-time performance, the global map is maintained using an incremental k-d tree structure (IkD-Tree). This structure allows for fast point insertion, deletion, and nearest-neighbor searches, which are essential for calculating point-to-map residuals and detecting loop closures. By processing the entire dataset collected during a measurement campaign, this framework generates a high-resolution, globally consistent 3D point cloud map, effectively creating a digital twin of the measurement environment.

D. Visual Data Fusion for Real-time Sensing

While the global 3D map provides a static environment representation, real-time sensing is essential for capturing dynamic scenarios and linking instantaneous channel behavior to specific objects. To this end, synchronized LiDAR point clouds and camera images are fused, combining the semantic richness of images for object detection with the precise 3D spatial information from point clouds.

The core of the fusion process is the projection of 3D points from the LiDAR coordinate system onto the 2D image plane. This requires precise extrinsic and intrinsic calibration. Let $\mathbf{P}_L = [X_L, Y_L, Z_L]^T$ be a point in the LiDAR's coordinate frame. First, it is transformed into the camera's coordinate frame $\mathbf{P}_C = [X_C, Y_C, Z_C]^T$ using the rigid body transformation matrix $\mathbf{T}_{C \leftarrow L}$, which represents the rotation $\mathbf{R}_{C \leftarrow L}$ and translation $\mathbf{t}_{C \leftarrow L}$ from LiDAR to camera:

$$\begin{bmatrix} \mathbf{P}_C \\ 1 \end{bmatrix} = \mathbf{T}_{C \leftarrow L} \begin{bmatrix} \mathbf{P}_L \\ 1 \end{bmatrix} = \begin{bmatrix} \mathbf{R}_{C \leftarrow L} & \mathbf{t}_{C \leftarrow L} \\ \mathbf{0}^T & 1 \end{bmatrix} \begin{bmatrix} \mathbf{P}_L \\ 1 \end{bmatrix}. \quad (6)$$

Next, the 3D point \mathbf{P}_C is projected onto the image plane to obtain the pixel coordinates $\mathbf{p} = [u, v]^T$ using the camera's intrinsic matrix \mathbf{K} :

$$Z_C \begin{bmatrix} u \\ v \\ 1 \end{bmatrix} = \mathbf{K} \mathbf{P}_C = \begin{bmatrix} f_x & 0 & c_x \\ 0 & f_y & c_y \\ 0 & 0 & 1 \end{bmatrix} \begin{bmatrix} X_C \\ Y_C \\ Z_C \end{bmatrix}, \quad (7)$$

where (f_x, f_y) are the focal lengths and (c_x, c_y) is the principal point of the camera.

As illustrated in Fig. 7, this projection technique allows us to accurately overlay LiDAR points onto the corresponding RGB image. In Fig. 7, point cloud is color-coded by distance, clearly visualizing the 3D structure of scenario, including ground plane, surrounding buildings, fences, and vehicles, directly on the 2D image. This fusion enables the association of semantic labels, derived from running 2D object detectors on the image (e.g., identifying the red car or building facade), with their corresponding 3D point clusters. Through this real-time data fusion, we achieve synchronized environmental sensing alongside our channel measurements. This capability allows us to precisely identify the 3D position and type of major reflectors and scatterers in the environment at any given moment. This enriched, multi-modal data stream provides the critical contextual information necessary for the subsequent joint analysis of channel-environment interactions.

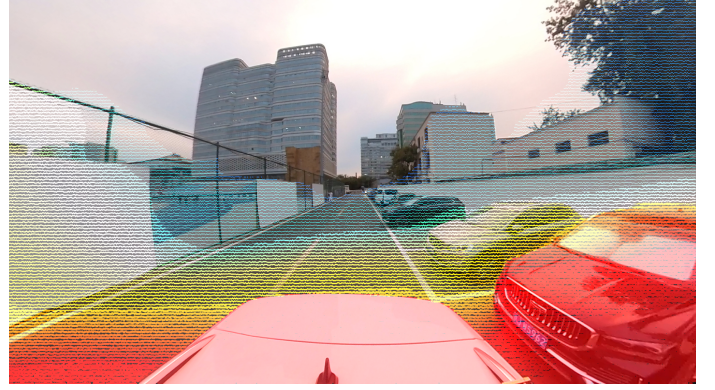


Fig. 7. Example of fusing a real-time LiDAR point cloud frame with a synchronized camera image. The points are colored by distance, providing depth perception overlaid on the visual scene.

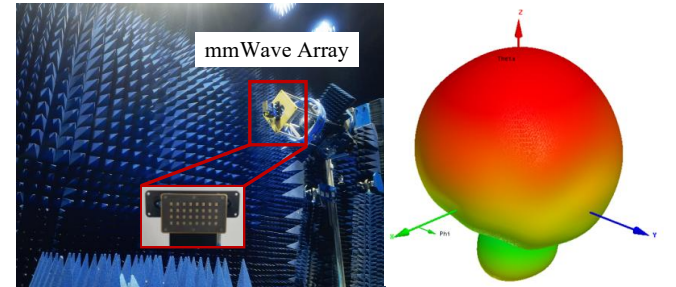


Fig. 8. Anechoic chamber measurement setup for characterization of the per-element gain and phase patterns of mmWave antenna array.

V. SYSTEM VERIFICATION

A. System Calibration

System calibration is crucial to ensure accuracy, repeatability, and spatial fidelity in channel measurements [42]. The procedure consists of three stages: instrument self-calibration, back-to-back (B2B) calibration, and antenna calibration. Instrument self-calibration compensates for hardware drift, temperature variation, and aging, with automated routines adjusting frequency references and modulators/demodulators before each measurement. B2B calibration eliminates system distortions by directly connecting Tx and Rx through attenuated RF cables, extracting the intrinsic system response for data compensation. Antenna calibration corrects directionality, gain, and polarization effects. Radiation patterns are measured in an anechoic chamber using azimuthal rotation, as shown in Fig. 8, and the results are used to normalize antenna gain and construct accurate steering vectors, thereby improving angle-domain parameter estimation. Fig. 9 shows the calibrated and uncalibrated amplitude responses, demonstrating that calibration process effectively eliminates frequency-dependent gain variations and smooths the overall response.

B. Dynamic Range

Fig. 10 presents the link budget analysis of the mmWave channel sounder. To estimate the maximum measurable propagation loss, a narrow-beam horn antenna with 30 dB gain is used at Tx, and a 32-element rectangular array is deployed at

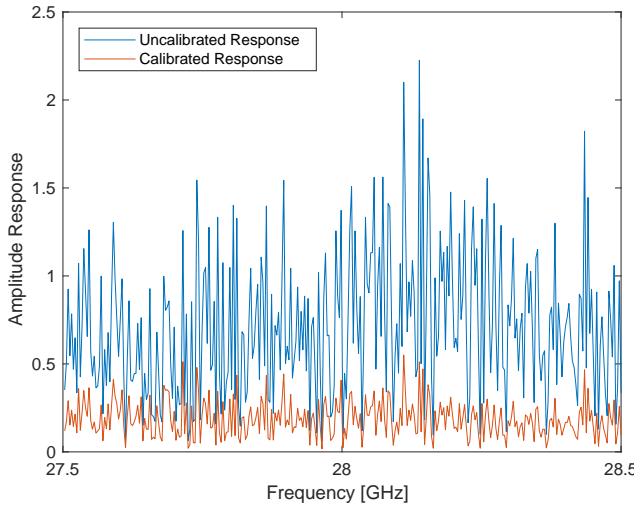


Fig. 9. Calibrated and uncalibrated amplitude responses of the system.

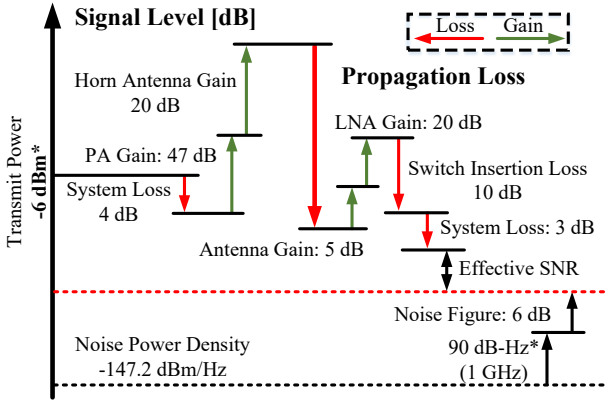


Fig. 10. Example of a link budget analysis for a mmWave channel sounder using a high-gain narrow-beam horn as the transmit antenna and a 32-element rectangular array at the receiver. “*” indicates adjustable value.

Rx. As shown in Fig. 10, Tx operates at maximum output, with the PXIE-5745 providing -6 dBm and PA gain of 47 dB, resulting in an effective transmit power of 75 dBm. At Rx, average gain of 5 dB is achieved due to the directivity of antenna array, with LNA gain of 20 dB. System-level hardware losses from interfaces and cables on Tx and Rx are 4 dB and 3 dB, respectively. Moreover, the insertion loss caused by electronic switching is 10 dB. Regarding noise power, the intrinsic noise spectral density of PXIE-5775 is -147.2 dBm/Hz , corresponding to a total noise power of -57.2 dBm over an effective bandwidth of 1 GHz (90 dB-Hz). Furthermore, the cascaded noise figure of Rx components is approximately 6 dB. Based on these parameters, the effective SNR and propagation loss can be derived. With the SNR threshold is 0 dB, the maximum measurable propagation loss is approximately 128.2 dB.

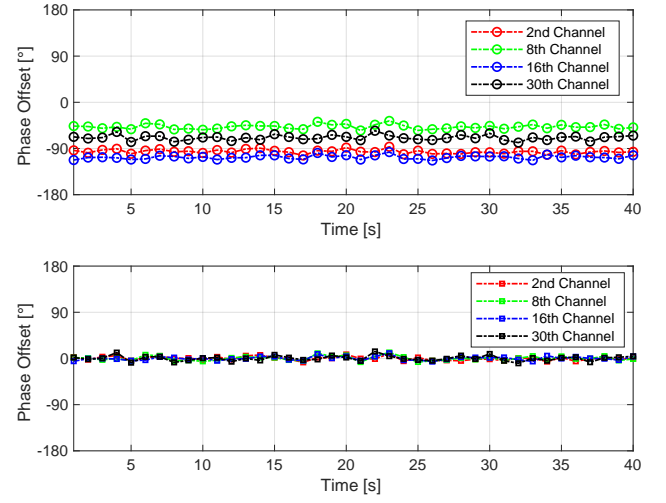


Fig. 11. Calibrated and uncalibrated phase offsets with respect to Channel 1.

C. Phase Stability

The stability of phase information plays a crucial role in multipath channel measurement and modeling. Any significant phase drift in the measurement system degrades delay resolution, distorts multipath parameter estimation, and causes inconsistencies among measurements over time, thereby reducing the reliability of the derived channel model. To ensure measurement accuracy, the long-term phase stability of the channel sounder is evaluated.

The experiment is conducted in a static indoor environment using the mmWave sounder as an example. In SIMO measurements, electronic switch introduces fixed phase offsets across different channels, which should remain stable over time to ensure system consistency. As shown in Fig. 11, the upper plot presents the uncalibrated phase offsets of multiple channels relative to Channel 1, where noticeable static offsets and random fluctuations can be observed. After applying calibration, as illustrated in the lower plot, these offsets are effectively compensated, and all channels exhibit highly consistent and stable phase responses with negligible drift over time. This demonstrates that the proposed calibration method successfully removes the inter-channel phase bias and enhances the phase stability of the sounder. Overall, the system maintains excellent synchronization performance, ensuring the accuracy and repeatability of channel measurements.

D. LiDAR Data Destaggering

As an active sensor, LiDAR provides high-precision 3D information about the surrounding environment. However, the raw LiDAR frames are not flawless and cannot be directly used for high-level perception tasks such as object detection or 3D reconstruction. A major inherent artifact is the staggering phenomenon. As shown in Fig. 12(a), the uncorrected LiDAR range image exhibits visible distortion, where vertical structures such as trees and poles appear tilted and jagged. This effect results from the mechanical scanning process and internal signal delays. Using such distorted data causes

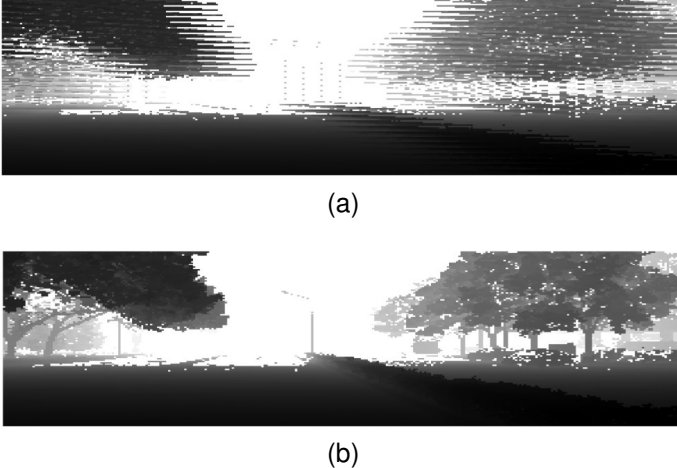


Fig. 12. Comparison of range grayscale images before and after destaggering correction. (a) Before destaggering. (b) After destaggering. Both images share a common grayscale map and display range, clamped to the 1-99 percentile. Zero or invalid ranges are masked in white.

perception algorithms to misinterpret vertical objects, leading to inaccurate feature extraction, failed edge detection, and degraded performance in localization, mapping, and obstacle avoidance. Therefore, geometric distortion correction is an essential preprocessing step.

The staggering artifact arises from a timing mismatch in LiDAR acquisition process. Within a single column, multiple laser firing and receiving channels (corresponding to the image rows) do not record measurements simultaneously. The cause can be attributed to two factors:

- **Scanning Mechanism:** The LiDAR sensor rotates at a constant angular velocity ω , acquiring a column of data at a fixed time interval Δt_{col} , which corresponds to an angular step of $\Delta\theta = \omega \Delta t_{\text{col}}$.
- **Hardware Latency:** Each vertical channel r experiences a small but constant firing delay τ_r relative to the base acquisition time of column due to sequential triggering.

Consequently, the sampling time $t_{r,c}$ for a pixel at (r, c) is given by:

$$t_{r,c} = t_0 + c \Delta t_{\text{col}} + \tau_r, \quad (8)$$

where t_0 denotes the frame start time. This delay τ_r introduces an azimuthal offset:

$$\Delta\theta_r = \omega \tau_r. \quad (9)$$

This means that even pixels in the same column have slightly different azimuth angles ($\theta_{r,c} = \theta_c + \Delta\theta_r$). This row-dependent angular shift causes vertical structures to appear slanted in the range image.

The goal of destaggering correction is to compensate for this inter-row azimuthal offset, ensuring that each image column corresponds to a single azimuth angle. The pre-calculated horizontal pixel offset s_r provided in the LiDAR metadata directly quantifies the deviation caused by τ_r . The correction is implemented as an independent horizontal circular shift for each row of the raw frame. Let the staggered frame be $S \in \mathbb{R}^{H \times W}$ and the corrected frame be $D \in \mathbb{R}^{H \times W}$, where

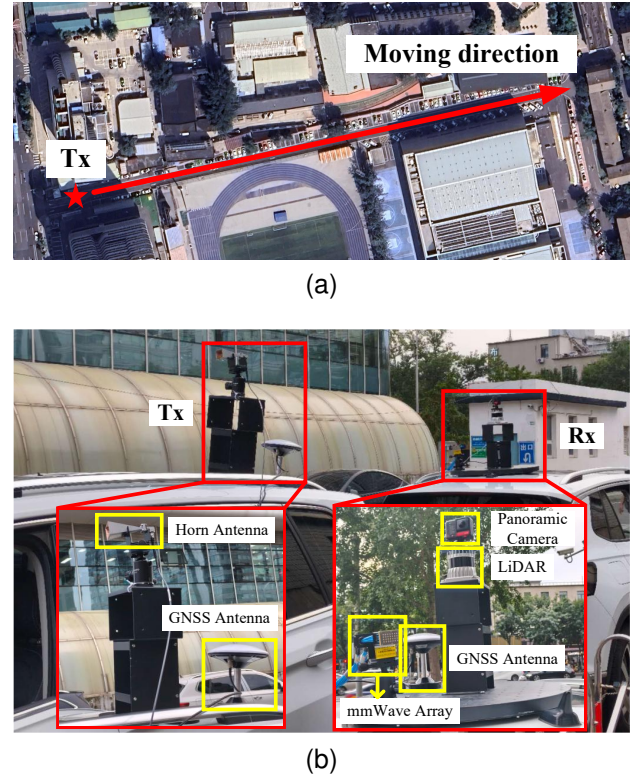


Fig. 13. (a) Measurement environment; (b) Measurement equipment.

H is the number of vertical channels and W is the number of columns per frame. The correction is defined as:

$$D[r, c] = S[r, (c + s_r) \bmod W]. \quad (10)$$

Here, the pixel at $[r, c]$ in the corrected image D is taken from the same row in S , shifted by s_r columns. The modulo operation ensures circular wrapping, which is essential for 360° panoramic scans. As shown in Fig. 12(b), after applying destaggering, vertical structures are properly aligned, and the geometric consistency of the scene is fully restored.

VI. SAMPLE MEASUREMENT

A. Measurement Campaign

To validate the performance of the proposed platform, we conduct a 28-GHz SIMO V2I measurement campaign with a measurement bandwidth of 1 GHz in a representative urban scenario, as illustrated in Fig. 13(a). The measurement route is a straight road approximately 400 m in length, with low walls and parked vehicles on the left side, and a low fence on the right. The environment contains no significant obstructions, apart from a few pedestrians and passing vehicles. Fig. 13(b) shows test vehicles and measurement equipment. At Tx, a narrow-beam horn antenna with an effective beamwidth of 12° – 19° is employed, while Rx is equipped with a 32-element array antenna. A custom-designed magnetic mount rigidly aligns the array with a LiDAR, panoramic camera, and GNSS antenna on the same horizontal plane, ensuring synchronized multi-modal data acquisition during mobility. Detailed hardware specifications are provided in Table. III.

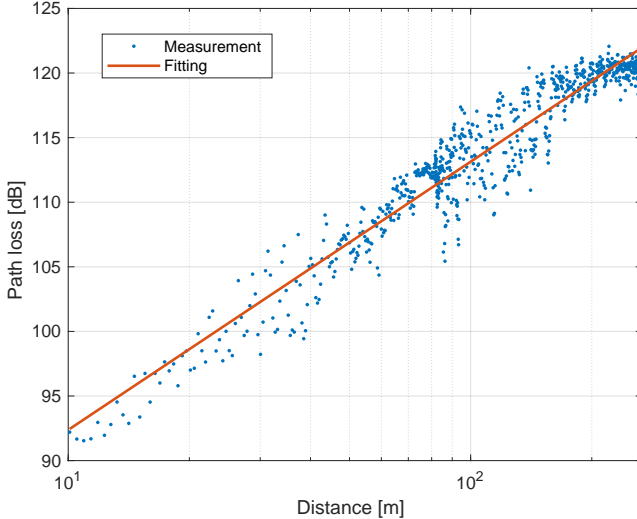


Fig. 14. The measured PL against Tx-Rx separation distance.

To maintain LoS conditions, two identical vehicles are deployed, with the transmitter vehicle kept stationary and the receiver vehicle traveling along the predefined trajectory at an average speed of 20 km/h. Rx collects SIMO channel data at a rate of 50 snapshots per second, and the entire measurement procedure is repeated five times to ensure sufficient channel sounding data for performance validation.

B. Path Loss Verification

PL is a representative large-scale propagation characteristic that quantifies the attenuation of radio waves over long distances (tens to hundreds of wavelengths) [42], which can be estimated from the average channel gain as follows:

$$PL = -10\log_{10}\left(\frac{1}{W} \sum_{T=t-\frac{W}{2}}^{t+\frac{W}{2}-1} \sum_{\tau=1}^{N_f} |h(T, \tau)|^2\right), \quad (11)$$

where N_f is the number of frequency points, PL is the path loss in dB scale, and W is a 40λ sliding window, λ denotes wavelength. Fig. 14 presents the measured PL against Tx-Rx separation distance, where the blue points denote individual measurements, the red line is log-distance fitting. It can be observed that the measured PL closely follows the log-distance model, with a path loss exponent (PLE) of approximately 2.07. It indicates that the platform can accurately capture the large-scale attenuation trend. The dynamic range of the system allows reliable measurements up to 280 m, with the maximum observed path loss around 122 dB. Compared with the theoretical measurable range of 128 dB derived from the link budget, this confirms that the platform maintains sufficient SNR margin across the entire measurement route.

C. Power Delay Profile and Multipath Evolution

Power-delay profile (PDP) is extensively employed to characterize the power levels of received paths with propagation

delays and to describe the distribution of multi-path components in measured environments. The instantaneous PDP is denoted as

$$P(t, \tau) = |h(t, \tau)|^2. \quad (12)$$

Fig. 15(a) illustrates the PDP evolution over the measurement campaign, where the horizontal axis denotes delay and the vertical axis indicates snapshot index. A dominant LoS component can be clearly observed, continuously tracked across more than 800 snapshots. In addition, several weaker NLoS components appear intermittently at different times, resulting in significant delay spreads. Fig. 15(b) shows a representative snapshot at 40 s, where 7 clusters are identified. The earliest and strongest clusters (Cluster 1 and 2) correspond to the LoS component and early reflections, while the later clusters (e.g., Cluster 5–7) represent weak reflections with delays exceeding 200 ns. This clearly demonstrates the extremely high temporal resolution of platform, enabling the identification of multipath components at nanosecond scale.

D. SAGE-Based Angle Estimation Verification

The angular resolution capability of the developed platform is further validated by applying the Space-Alternating Generalized Expectation-maximization (SAGE) algorithm to extract the angles of arrival (AoAs). Fig. 15(c) shows the estimated azimuth over the measurement duration, with color indicating the relative power of multipath components. The azimuthal distribution is primarily concentrated within 80° – 140° , with a dominant and stable LoS trajectory observed near 100° throughout the 30–100 s measurement period. In addition to this strong component, several weaker reflections appear intermittently around 70° and 150° , reflecting the influence of dynamic roadside scatterers. Notably, even when weaker paths exhibit a power difference exceeding 20–30 dB compared with the dominant LoS, the system still resolves them. This confirms the high dynamic range and angular resolution.

E. Multi-modal Data Verification

To further validate the reliability and interpretability of developed platform, we have conducted multi-modal data fusion by integrating wireless measurement results with synchronized camera and LiDAR information. Fig. 16 presents two representative snapshots at 5 s and 20 s. At 5-th s, the LoS component is clearly observed, with an elevation angle of approximately 150° , corresponding to TX. In addition, a prominent reflection cluster arises from the building wall on the right-hand side, while the ground-reflected components are concentrated within the elevation range of 40° – 60° . The camera and LiDAR evidence enable a precise mapping between scattering objects and the wireless measurement results. At 20 s, the LoS component is still present, but compared with the 5 s snapshot, its angular position shifts slightly toward the center. This change is consistent with the relative motion of the receiver vehicle with respect to the transmitter, demonstrating the platform's capability of dynamic LoS tracking. Meanwhile, beyond the wall reflection, additional multipath clusters corresponding to parked vehicles appear in the 60° – 80° elevation region,

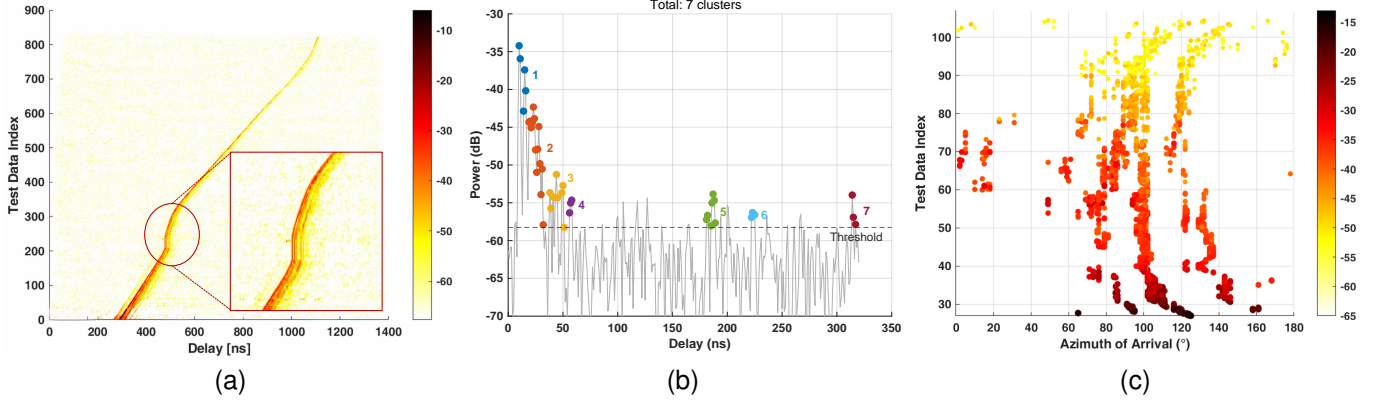


Fig. 15. (a) The PDP evolution over the measurement campaign; (b) Multipath clustering results based on the measured PDP; (c) SAGE-based angle-of-arrival estimation results over the measurement campaign.



Fig. 16. Multi-modal verification combining wireless channel sounding, camera, and LiDAR data.

with power levels about 20 dB weaker than the LoS but still reliably detected. Overall, the platform is capable of capturing multipath evolution and mapping it to physical environments through multi-modal information, highlighting its advanced features and practical value for ISAC applications.

VII. CONCLUSION

In this paper, we present a multi-modal environment sensing and channel sounding platform designed to address the limitations of traditional channel sounders in highly dynamic 6G scenarios. By integrating diverse sensing devices and channel sounders, the platform enables temporally and spatially synchronized acquisition of multi-modal data, including images, point clouds, GNSS, and multi-band channel data. The performance of platform has been verified through V2I channel measurements. The platform supports Sub-6 GHz and 27-29 GHz with up to 1 GHz bandwidth, 1 ns delay resolution, and 8 ms antenna switching, while achieving centimeter-level 360° environmental sensing and meter-level positioning accuracy. It

ensures reliable identification of multipath clusters and their multi-modal mapping to real-world environments. The platform establishes a comprehensive experimental foundation for investigating the interplay between physical environments and wireless channels under high-mobility conditions. Moreover, it is expected to serve as a valuable research infrastructure for advancing environment-aware paradigms in 6G systems.

REFERENCES

- [1] R. He and B. Ai, *Wireless Channel Measurement and Modeling in Mobile Communication Scenario: Theory and Application*. CRC Press, 2024.
- [2] Z. Zhang *et al.*, “A general channel model for integrated sensing and communication scenarios,” *IEEE Commun. Mag.*, vol. 61, no. 5, pp. 68–74, 2023.
- [3] C. Huang *et al.*, “Artificial intelligence enabled radio propagation for communications—Part I: Channel characterization and antenna-channel optimization,” *IEEE Trans. Antennas Propag.*, vol. 70, no. 6, pp. 3939–3954, 2022.
- [4] ITU-R, “Future technology trends of terrestrial International Mobile

- Telecommunications systems towards 2030 and beyond," *Report M.2516-0*, Nov. 2022. [Online]. Available: https://www.itu.int/dms_pub/itu-r/opb/rep/R-REP-M.2516-2022-PDF-E.pdf
- [5] ITU-R, "Framework and overall objectives of the future development of IMT for 2030 and beyond," *DRAFT NEW RECOMMENDATION*, Jun. 2023.
- [6] COST CA20120 Action, "INTERACT: Intelligence-enabling radio communications for seamless inclusive interactions," 2021. [Online]. Available: <https://www.cost.eu/actions/CA20120>
- [7] X. Cheng *et al.*, "Intelligent multi-modal sensing-communication integration: Synesthesia of machines," *IEEE Commun. Surveys Tuts.*, vol. 26, no. 1, pp. 258–301, 2024.
- [8] R. He and Z. Ding, *Applications of machine learning in wireless communications*. London, U.K: Inst. Eng. Technol., Jul. 2019.
- [9] X. Zhang, R. He, M. Yang, Z. Zhang, Z. Qi, and B. Ai, "Vision aided channel prediction for vehicular communications: A case study of received power prediction using RGB images," *IEEE Trans. Veh. Technol.*, vol. 74, no. 11, pp. 17531–17544, 2025.
- [10] R. He, M. Yang, Z. Zhang, B. Ai, and Z. Zhong, "Artificial intelligence empowered channel prediction: A new paradigm for propagation channel modeling," *arXiv preprint arXiv:2601.09205*, 2026.
- [11] L. Bai, Z. Huang, M. Sun, X. Cheng, and L. Cui, "Multi-modal intelligent channel modeling: A new modeling paradigm via synesthesia of machines," *IEEE Commun. Surveys Tuts.*, pp. 1–1, 2025.
- [12] T. Nishio, Y. Koda, J. Park, M. Bennis, and K. Doppler, "When wireless communications meet computer vision in beyond 5G," *IEEE Commun. Standards Mag.*, vol. 5, no. 2, pp. 76–83, 2021.
- [13] X. Zhang, R. He, M. Yang, Z. Qi, Z. Zhang, B. Ai, and Z. Zhong, "Vision-aided channel prediction based on image segmentation at street intersection scenarios," *IEEE Trans. on Cogn. Commun. Netw.*, vol. 12, pp. 1678–1693, 2026.
- [14] Z. Zhang *et al.*, "Non-stationarity characteristics in dynamic vehicular ISAC channels at 28 GHz," *Chinese J. Electron.*, vol. 34, no. 1, pp. 73–81, 2025.
- [15] S. Imran, G. Charan, and A. Alkhateeb, "Environment semantic communication: Enabling distributed sensing aided networks," *IEEE Open J. Commun. Soc.*, vol. 5, pp. 7767–7786, 2024.
- [16] Z. Zhang *et al.*, "Deep learning-based human gesture channel modeling for integrated sensing and communication scenarios," *IEEE Trans. Antennas Propag.*, pp. 1–1, 2025.
- [17] F. Wen, W. Xu, F. Gao, C. Pan, and G. Liu, "Vision aided environment semantics extraction and its application in mmWave beam selection," *IEEE Commun. Lett.*, vol. 27, no. 7, pp. 1894–1898, 2023.
- [18] Y. Yang, F. Gao, X. Tao, G. Liu, and C. Pan, "Environment semantics aided wireless communications: A case study of mmWave beam prediction and blockage prediction," *IEEE J. Sel. Areas Commun.*, vol. 41, no. 7, pp. 2025–2040, 2023.
- [19] R. He *et al.*, "Propagation channels of 5G millimeter-wave vehicle-to-vehicle communications: Recent advances and future challenges," *IEEE Veh. Technol. Mag.*, vol. 15, no. 1, pp. 16–26, 2020.
- [20] R. He, N. D. Cicco, B. Ai, M. Yang, Y. Miao, and M. Boban, "COST CA20120 INTERACT framework of artificial intelligence-based channel modeling," *IEEE Wirel. Commun.*, vol. 32, no. 4, pp. 200–207, 2025.
- [21] C. Huang *et al.*, "Artificial intelligence enabled radio propagation for communications—part II: Scenario identification and channel modeling," *IEEE Trans. Antennas Propag.*, vol. 70, no. 6, pp. 3955–3969, 2022.
- [22] Z. Zhang *et al.*, "A cluster-based statistical channel model for integrated sensing and communication channels," *IEEE Trans. Wireless Commun.*, vol. 23, no. 9, pp. 11597–11611, 2024.
- [23] M. Sandra, C. Nelson, X. Li, X. Cai, F. Tufvesson, and A. J. Johansson, "A wideband distributed massive mimo channel sounder for communication and sensing," *IEEE Trans. Antennas Propag.*, vol. 73, no. 4, pp. 2074–2085, 2025.
- [24] Y. Wang, W. Wang, Y. Wu, J. Liu, Q. Zhang, J. Wang, and W. Fan, "USRP-based multifrequency multiscenario channel measurements and modeling for 5G campus internet of things," *IEEE Internet Things J.*, vol. 11, no. 8, pp. 13865–13883, 2023.
- [25] C. U. Bas, V. Kristem, R. Wang, and A. F. Molisch, "Real-time ultra-wideband channel sounder design for 3–18 GHz," *IEEE Trans. Commun.*, vol. 67, no. 4, pp. 2995–3008, 2018.
- [26] X. Cai, E. L. Bengtsson, O. Edfors, and F. Tufvesson, "A switched array sounder for dynamic millimeter-wave channel characterization: Design, implementation, and measurements," *IEEE Trans. Antennas Propag.*, vol. 72, no. 7, pp. 5985–5999, 2024.
- [27] C. U. Bas *et al.*, "Real-time millimeter-wave MIMO channel sounder for dynamic directional measurements," *IEEE Trans. Veh. Technol.*, vol. 68, no. 9, pp. 8775–8789, 2019.
- [28] X. Cai, G. Zhang, C. Zhang, W. Fan, J. Li, and G. F. Pedersen, "Dynamic channel modeling for indoor millimeter-wave propagation channels based on measurements," *IEEE Trans. Commun.*, vol. 68, no. 9, pp. 5878–5891, 2020.
- [29] A. Al-Ameri, J. Sanchez, F. Tufvesson, and X. Cai, "A fast rotating-mirror sounder for dynamic millimeter-wave channel characterization," in *Proc. IEEE 100th Veh. Technol. Conf.*, 2024, pp. 1–5.
- [30] J. Huang, C.-X. Wang, H. Chang, J. Sun, and X. Gao, "Multi-frequency multi-scenario millimeter wave MIMO channel measurements and modeling for B5G wireless communication systems," *IEEE J. Sel. Areas Commun.*, vol. 38, no. 9, pp. 2010–2025, 2020.
- [31] K. Mao *et al.*, "A UAV-aided real-time channel sounder for highly dynamic nonstationary A2G scenarios," *IEEE Trans. Instrum. Meas.*, vol. 72, pp. 1–15, 2023.
- [32] C. Chen, D. Fei, P. Zheng, and B. Ai, "A passive channel measurement and analysis based on a 5G commercial network in V2I communications," *Electronics*, vol. 12, no. 17, p. 3715, 2023.
- [33] T. Wu, X. Yin, L. Zhang, and J. Ning, "Measurement-based channel characterization for 5G downlink based on passive sounding in sub-6 GHz 5G commercial networks," *IEEE Trans. Wireless Commun.*, vol. 20, no. 5, pp. 3225–3239, 2021.
- [34] H. Miao, J. Zhang, P. Tang, L. Tian, X. Zhao, B. Guo, and G. Liu, "Sub-6 GHz to mmwave for 5G-advanced and beyond: Channel measurements, characteristics and impact on system performance," *IEEE J. Sel. Areas Commun.*, vol. 41, no. 6, pp. 1945–1960, 2023.
- [35] M. Kim, H. Tsukada, K. Kumakura, R. Takahashi, N. Suzuki, H. Sawada, and T. Matsumura, "A 24/60-GHz dual-band double-directional channel sounder using COTS phased arrays," in *Proc. IEEE Int. Conf. Commun. Workshops (ICC Workshops)*, 2022, pp. 1113–1117.
- [36] C. Gentile, J. Senic, A. Bodi, S. Berweger, R. Caromi, and N. Golmie, "Context-aware channel sounder for AI-assisted radio-frequency channel modeling," in *Proc. 18th Eur. Conf. Antennas Propag. (EuCAP)*, 2024, pp. 1–5.
- [37] A. Alkhateeb, G. Charan, T. Osman, A. Hredzak, J. Morais, U. Demirhan, and N. Srinivas, "Deepsense 6G: A large-scale real-world multi-modal sensing and communication dataset," *IEEE Commun. Mag.*, vol. 61, no. 9, pp. 122–128, 2023.
- [38] X. Zhang, R. He, M. Yang, Z. Qi, Z. Zhang, B. Ai, and R. Chen, "Narrowband channel measurements and statistical characterization in subway tunnels at 1.8 and 5.8 GHz," *IEEE Trans. Veh. Technol.*, vol. 73, no. 7, pp. 10228–10240, 2024.
- [39] G. Charan and A. Alkhateeb, "User identification: A key enabler for multi-user vision-aided communications," *IEEE Open J. Commun. Society*, vol. 5, pp. 472–488, 2024.
- [40] D. Fei, C. Chen, P. Zheng, D. Zhang, J. Yang, H. Chen, and B. Ai, "A novel millimeter-wave channel measurement platform for 6G intelligent railway scenarios," *China Commun.*, vol. 19, no. 11, pp. 60–73, 2022.
- [41] Z. Qi *et al.*, "Point cloud-based environment reconstruction and ray tracing simulations for railway tunnel channels," *High-speed Railway*, vol. 1, no. 4, pp. 241–247, 2023.
- [42] X. Zhang *et al.*, "Measurements and modeling of large-scale channel characteristics in subway tunnels at 1.8 and 5.8 GHz," *IEEE Antennas Wireless Propag. Lett.*, vol. 22, no. 3, pp. 561–565, 2023.